2HDM AND ENHANCED RATES IN $\gamma\gamma$ CHANNEL*

Aleksandra Drozd[a,b], Bohdan Grzadkowski[a]
John F. Gunion[b], Yun Jiang[b]

[a]Faculty of Physics, University of Warsaw, 00-681 Warszawa, Poland,
[b]Department of Physics, University of California, Davis, CA 95616, USA

(Received June 3, 2013)

We examine maximum enhancement that can be achieved in the ZZ and $\gamma\gamma$ channels for a two-Higgs-doublet model Higgs boson with a mass near 125 GeV. Theoretical constraints restrict substantially the possibilities for enhancing the $gg \to h \to \gamma\gamma$ or $gg \to H \to \gamma\gamma$ signal relative to that for the SM Higgs. We find enhanced rates in the $\gamma\gamma$ final state for the h in the Type I 2HDM — the largest $[gg \to h \to \gamma\gamma]/[gg \to h_{\mathrm{SM}}\gamma\gamma]$ ratio found is of the order of ~ 1.3, when $\tan\beta = 4$ or 20 and the charged Higgs boson has its minimal LEP-allowed value of $m_{H^\pm} = 90$ GeV.

DOI:10.5506/APhysPolB.44.1417
PACS numbers: 12.60.Fr, 14.80.Ec, 14.80.Fd

1. Introduction

Data from the ATLAS and CMS collaborations [1, 2] provided an essentially 5σ signal for a Higgs-like resonance with mass of the order of 123–128 GeV. In the $\gamma\gamma$ final state, the ATLAS and CMS gluon fusion induced rates are significantly enhanced relative to the Standard Model (SM) prediction.

Enhancements with respect to the SM in the $\gamma\gamma$ channel are generically possible in two-Higgs-doublet models (2HDM) of the Type I and Type II as explored in [3–8]. In this paper, we impose all constraints from B-physics and LEP data (B/LEP), precision electroweak data, stability, unitarity and perturbativity to determine the maximum possible enhancement, considering also cases of degenerate scalar masses at ~ 125 GeV [9].

* Presented at the Cracow Epiphany Conference on the Physics After the First Phase of the LHC, Kraków, Poland, January 7–9, 2013.

2. 2HDM models

The general Higgs sector potential employed is

$$
\begin{aligned}
\mathcal{V} \;=\; & m_{11}^2\Phi_1^\dagger\Phi_1 + m_{22}^2\Phi_2^\dagger\Phi_2 - \left[m_{12}^2\Phi_1^\dagger\Phi_2 + \text{h.c.}\right] + \tfrac{1}{2}\lambda_1\left(\Phi_1^\dagger\Phi_1\right)^2 \\
& + \tfrac{1}{2}\lambda_2\left(\Phi_2^\dagger\Phi_2\right)^2 + \lambda_3\left(\Phi_1^\dagger\Phi_1\right)\left(\Phi_2^\dagger\Phi_2\right) + \lambda_4\left(\Phi_1^\dagger\Phi_2\right)\left(\Phi_2^\dagger\Phi_1\right) \\
& + \left\{\tfrac{1}{2}\lambda_5\left(\Phi_1^\dagger\Phi_2\right)^2 + \left[\lambda_6\left(\Phi_1^\dagger\Phi_1\right) + \lambda_7\left(\Phi_2^\dagger\Phi_2\right)\right]\left(\Phi_1^\dagger\Phi_2\right) + \text{h.c.}\right\}, \qquad (1)
\end{aligned}
$$

where, to avoid explicit $\mathcal{CP}$ violation in the Higgs sector, all λ_i and m_{12}^2 are assumed to be real. We choose a basis in which

$$
\langle\Phi_1\rangle = \frac{v}{\sqrt{2}}\begin{pmatrix} 0 \\ \cos\beta \end{pmatrix}, \qquad \langle\Phi_2\rangle = \frac{v}{\sqrt{2}}\begin{pmatrix} 0 \\ e^{i\xi}\sin\beta \end{pmatrix},
$$

where $v = (\sqrt{2}G_\text{F})^{-1/2} \approx 246$ GeV, $0 \leq \beta \leq \pi/2$ is chosen and we take $\xi = 0$ (no $\mathcal{CP}$ violation). Then, we define

$$
\Phi_a = \begin{pmatrix} \phi_a^+ \\ (v_a + \rho_a + i\eta_a)/\sqrt{2} \end{pmatrix}, \qquad a = 1,2 \tag{2}
$$

with $v_1 = v\cos\beta$ and $v_2 = v\sin\beta$. The neutral Goldstone boson is $G^0 = \eta_1\cos\beta + \eta_2\sin\beta$, while the physical pseudoscalar state and the physical scalars are

$$
A = -\eta_1\sin\beta + \eta_2\cos\beta\,, \tag{3}
$$

$$
h = -\rho_1\sin\alpha + \rho_2\cos\alpha\,, \qquad H = \rho_1\cos\alpha + \rho_2\sin\alpha\,. \tag{4}
$$

Without loss of generality, one can assume that the mixing angle α varies between $-\pi/2$ and $\pi/2$. We choose our independent variables to be $\tan\beta$ and $\sin\alpha$, which are single-valued in the allowed ranges.

We discuss the Type I and Type II 2HDM models that are defined by the fermion coupling patterns as specified in [12].

We adopt the code 2HDMC [10] for numerical calculations[1]. For input parameters, we use the physical Higgs boson masses $(m_H, m_h, m_A, m_{H^\pm})$, $\tan\beta$, $\sin\alpha$ and m_{12}^2, with λ_6 and λ_7 assumed to be zero (in view of Z_2 symmetry). With the above inputs, $\lambda_{1,2,3,4,5}$, m_{11}^2 and m_{22}^2 are determined [11].

[1] We have modified the subroutine in 2HDMC that calculates the Higgs boson decays to $\gamma\gamma$ and also the part of the code relevant for QCD corrections to the $q\bar{q}$ final state.

3. Setup of the analysis

The 2HDMC code implements precision electroweak constraints (denoted STU) and theoretical constraints: vacuum stability, unitarity and coupling-constant perturbativity (denoted jointly as SUP). By coupling constant perturbativity, we mean the requirement that all self-couplings among the Higgs-boson mass eigenstates are smaller than 4π (this becomes an important constraint on λ_1). Vacuum stability is the requirement of positivity of the potential in all directions at asymptotically large field strength. Unitarity is the requirement that the multi-channel Higgs scattering matrix have a largest eigenvalue below the unitarity limit using the analysis of [16]. The SUP constraints are particularly crucial in limiting the level of enhancement of the $gg \to h \to \gamma\gamma$ channel.

We have also included the B/LEP constraints and for the LEP data we adopt upper limits on $\sigma(e^+e^- \to Z\,h/H)$ and $\sigma(e^+e^- \to A\,h/H)$ from [13] and [14], respectively. Regarding B-physics, the constraints imposed are those from $\mathrm{BR}(B_s \to X_s\gamma)$, R_b, ΔM_{B_s}, ϵ_K, $\mathrm{BR}(B^+ \to \tau^+\nu_\tau)$ and $\mathrm{BR}(B^+ \to D\tau^+\nu_\tau)$. B-physics constraints allow us to place a lower bound on $m_{H^\pm}$ as a function of $\tan\beta$ as shown in Fig. 18 and Fig. 15 of [15] in the case of the Type I and Type II model, respectively. However, we ignore the anomalous magnetic moment of the muon $(g-2)_\mu$ as its 2HDM contribution δa_μ is very small unless $\tan\beta$ is of the order of 100.

For an individual Higgs, denoted h_i (where $h_i = h, H, A$ are the choices), we compute the ratio of the gg or WW-fusion (VBF) induced Higgs cross section times the Higgs branching ratio to a given final state, X, relative to the corresponding value for the SM Higgs boson, h_{SM}, as follows

$$
\begin{aligned}
R^{h_i}_{gg}(X) &\equiv \left(C^{h_i}_{gg}\right)^2 \frac{\mathrm{BR}(h_i \to X)}{\mathrm{BR}(h_{\mathrm{SM}} \to X)}\,, \\
R^{h_i}_{\mathrm{VBF}}(X) &\equiv \left(C^{h_i}_{WW}\right)^2 \frac{\mathrm{BR}(h_i \to X)}{\mathrm{BR}(h_{\mathrm{SM}} \to X)}\,,
\end{aligned} \tag{5}
$$

where h_{SM} is the SM Higgs boson with $m_{h_{\mathrm{SM}}} = m_{h_i}$ and $C^{h_i}_{gg}, C^{h_i}_{WW}$ are the ratios of the $gg \to h_i$, $WW \to h_i$ couplings (C^A_{WW} being zero at tree level) to those for the SM, respectively. When considering degenerate cases of more than one h_i with mass 125 GeV [9], we sum the different R^{h_i} for the production/decay channel of interest.

We have performed five scans over the parameter space with the range of variation specified in Table I. The lower bound on $m_{H^\pm}$ for a given $\tan\beta$ is read off from Fig. 18 and Fig. 15 of [15].

TABLE I

Range of parameters adopted in the scans. The lower bound on $m_{H^\pm}$ for a given $\tan\beta$ is read off from Fig. 18 and Fig. 15 of [15].

	Scenario I	Scenario II
m_h [GeV]	125	$\{10,\ldots, 124.9\}$
m_H [GeV]	$125 + \{0.1, \ldots, 1000\}$	125
m_A [GeV]	$\{10, \ldots, 1000\}$	$\{10, \ldots, 1000\}$
$\tan\beta$	$\{0.5, \ldots, 20\}$	
$\sin\alpha$	$\{-1, \ldots, 1\}$	
m_{12}^2 [GeV^2]	$\{-1000^2, \ldots, 1000^2\}$	

	Scenario III	Scenario IV	Scenario V
m_h [GeV]	125	125	$\{10, \ldots, 124.9\}$
m_H [GeV]	125.1	$125 + \{0.1, \ldots, 1000\}$	125
m_A [GeV]	$\{10,\ldots,1000\}$	125.1	125.1
$\tan\beta$	$\{0.5, \ldots, 20\}$		
$\sin\alpha$	$\{-1, \ldots, 1\}$		
m_{12}^2 [GeV^2]	$\{-1000^2, \ldots, 1000^2\}$		

3.1. *The $m_h = 125$ GeV or $m_H = 125$ GeV scenarios*

For the case of h with mass $m_h = 125$ GeV, we scan over the masses of the other Higgs eigenstates (degenerate cases are discussed in the following section) and plot the maximum value achieved for the ratio $R^h_{gg}(\gamma\gamma)$ as a function of $\tan\beta$, see Fig. 1. These maximum values are plotted both prior to imposing any constraints and after imposing various combinations of the constraints (see Fig. 1, legend). For most values of $\tan\beta$ the B/LEP and STU precision electroweak constraints, both individually and in combination, leave the maximum $R^h_{gg}(\gamma\gamma)$ unchanged relative to a full scan over all of parameter space. In contrast, the SUP constraints greatly reduce the maximum value of $R^h_{gg}(\gamma\gamma)$.

After imposing all constraints, we see that in the Type I model maximum $R^h_{gg}(\gamma\gamma)$ values much above 1.3 are not possible. In the Type II model, maximum $R^h_{gg}(\gamma\gamma)$ values in the range of 2–3 are possible for $2 \leq \tan\beta \leq 7$ and $\tan\beta = 20$. Tables II and III display the full set of input parameters corresponding to the maximal $R^h_{gg}(\gamma\gamma)$ values at each $\tan\beta$ for models of Type I and Type II, respectively. It is important to notice that in the Type II model, the value of $R^h_{gg}(ZZ)$ corresponding to the parameters that maximize $R^h_{gg}(\gamma\gamma)$ is typically large, ~ 3.

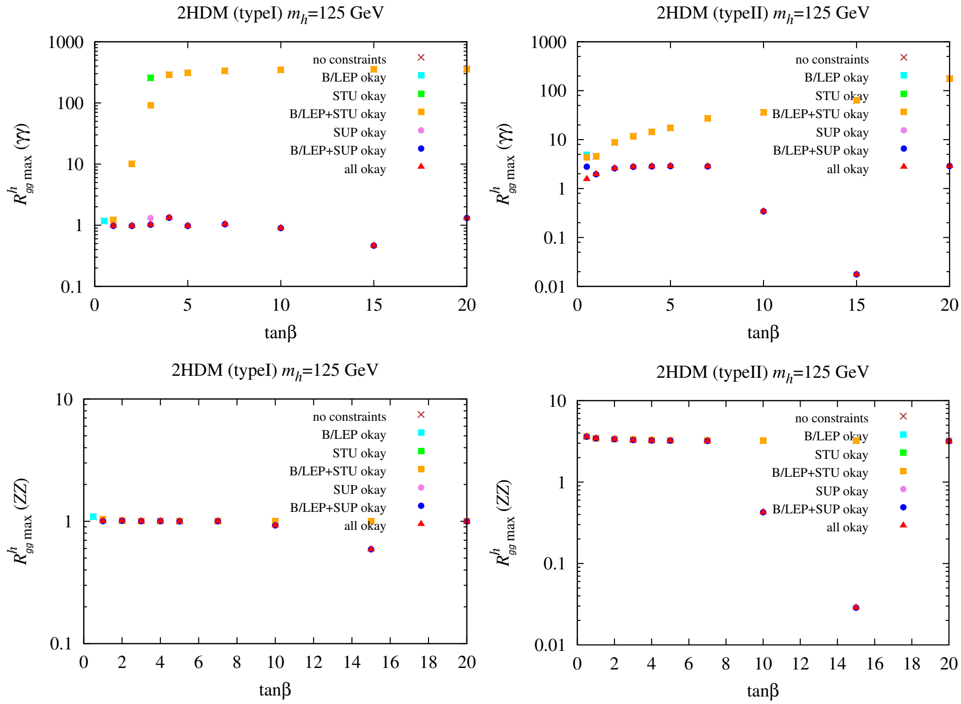

Fig. 1. The top two plots show the maximum $R^h_{gg}(\gamma\gamma)$ values in the Type I (left) and Type II (right) models for $m_h = 125$ GeV as a function of $\tan\beta$ after imposing various constraints — see the figure legend. Corresponding $R^h_{gg}(ZZ)$ values are shown in the lower panel. Disappearance of a point after imposing a given constraint set means that the point did not satisfy that set of constraints. In the case of boxes and circles, if a given point satisfies subsequent constraints, then the resulting color is chosen according to the color ordering shown in the legend, the same pattern is adopted in the remaining plots.

Corresponding results for the case of H with mass $m_H = 125$ GeV are presented for the Type I and Type II models in Tables IV and V, respectively. In the case of the Type I model, an enhanced gluon fusion rate in the $\gamma\gamma$ final state does not seem to be possible after imposing the SUP constraints. For the Type II model, maximal enhancements of the order of $R^H_{gg}(\gamma\gamma) \sim 2.8$ are quite typical, albeit with even larger $R^H_{gg}(ZZ)$.

In Type II models, we observe that an enhanced $\gamma\gamma$ rate (*e.g.* $R^{h,H}_{gg}(\gamma\gamma) > 1.2$) leads to $R^{h,H}_{gg}(\gamma\gamma)/R^{h,H}_{gg}(ZZ) < 1$, therefore, this case seems to be disfavored. An explanation of the mechanism behind the enhancement of $R^{h,H}_{gg}(ZZ)$ in the Type II model can be found in [5].

TABLE II

Table of maximum $R^h_{gg}(\gamma\gamma)$ values for the Type I 2HDM with $m_h = 125$ GeV and associated R values for other initial and/or final states. The input parameters that give the maximal $R^h_{gg}(\gamma\gamma)$ value are also tabulated.

$\tan\beta$	$R^h_{gg\max}(\gamma\gamma)$	$R^h_{gg}(ZZ)$	$R^h_{gg}(b\bar{b})$	$R^h_{\rm VBF}(\gamma\gamma)$	$R^h_{\rm VBF}(ZZ)$	$R^h_{\rm VBF}(b\bar{b})$	m_H	m_A	$m_{H^\pm}$	m_{12}	$\sin\alpha$	$\mathcal{A}^h_{H^\pm}/\mathcal{A}$
1.0	0.98	1.00	1.02	0.96	0.98	1.00	875	750	800	500	−0.7	−0.01
2.0	0.98	0.98	0.92	1.04	1.04	0.98	425	500	350	200	−0.5	−0.01
3.0	1.02	0.98	0.92	1.08	1.04	0.98	225	400	150	100	−0.4	0.01
4.0	1.33	0.99	1.07	1.24	0.93	0.99	225	200	90	100	−0.1	0.14
5.0	0.98	0.98	1.06	0.90	0.91	0.98	225	400	150	100	−0.0	0.01
7.0	1.04	0.99	0.98	1.06	1.01	0.99	135	500	90	50	−0.2	0.02
10.0	0.90	0.81	0.74	0.99	0.89	0.81	175	500	150	50	−0.5	0.04
15.0	0.46	0.59	0.66	0.41	0.53	0.59	225	400	350	50	0.6	−0.11
20.0	1.31	1.00	1.00	1.30	0.99	1.00	225	200	90	50	−0.0	0.13

TABLE III

Table of maximum $R^h_{gg}(\gamma\gamma)$ values for the Type II 2HDM with $m_h = 125$ GeV and associated R values for other initial and/or final states. The input parameters that give the maximal $R^h_{gg}(\gamma\gamma)$ value are also tabulated.

$\tan\beta$	$R^h_{gg\max}(\gamma\gamma)$	$R^h_{gg}(ZZ)$	$R^h_{gg}(b\bar{b})$	$R^h_{\rm VBF}(\gamma\gamma)$	$R^h_{\rm VBF}(ZZ)$	$R^h_{\rm VBF}(b\bar{b})$	m_H	m_A	$m_{H^\pm}$	m_{12}	$\sin\alpha$	$\mathcal{A}^h_{H^\pm}/\mathcal{A}$
0.5	1.56	2.69	1.84	0.52	0.89	0.61	425	500	600	100	−0.7	−0.06
1.0	1.97	3.36	0.39	0.65	1.11	0.13	125	500	500	100	−0.2	−0.06
2.0	2.59	3.36	0.00	1.48	1.92	0.00	225	200	340	100	−0.0	−0.05
3.0	2.78	3.29	0.00	2.01	2.37	0.00	225	200	320	100	−0.0	−0.05
4.0	2.84	3.25	0.00	2.24	2.57	0.00	225	200	320	100	−0.0	−0.04
5.0	2.87	3.23	0.00	2.37	2.66	0.00	225	200	320	100	−0.0	−0.04
7.0	2.83	3.21	0.00	2.42	2.75	0.00	135	300	320	50	−0.0	−0.05
10.0	0.34	0.43	1.89	0.22	0.28	1.23	325	200	320	100	0.2	−0.08
15.0	0.02	0.03	4.06	0.00	0.01	0.87	225	200	320	50	0.6	−0.14
20.0	2.89	3.19	0.00	2.57	2.83	0.00	225	200	320	50	−0.0	−0.04

TABLE IV

Table of maximum $R_{gg}^{H}(\gamma\gamma)$ values for the Type I 2HDM with $m_H = 125$ GeV and associated R values for other initial and/or final states. The input parameters that give the maximal $R_{gg}^{H}(\gamma\gamma)$ value are also tabulated.

$\tan\beta$	$R_{gg\max}^{H}(\gamma\gamma)$	$R_{gg}^{H}(ZZ)$	$R_{gg}^{H}(b\bar{b})$	$R_{\mathrm{VBF}}^{H}(\gamma\gamma)$	$R_{\mathrm{VBF}}^{H}(ZZ)$	$R_{\mathrm{VBF}}^{H}(b\bar{b})$	m_h	m_A	$m_{H^\pm}$	m_{12}	$\sin\alpha$	$\mathcal{A}_{H^\pm}^{H}/\mathcal{A}$
2.0	0.90	1.00	1.02	0.89	0.99	1.00	125	400	350	50	0.9	−0.05
3.0	0.89	0.96	0.88	0.97	1.05	0.96	125	400	350	50	0.9	−0.05
4.0	0.89	0.97	1.09	0.79	0.86	0.97	105	500	90	50	1.0	−0.03
5.0	0.93	0.98	1.06	0.86	0.90	0.98	125	500	90	50	1.0	−0.01
7.0	0.88	0.99	1.03	0.85	0.95	0.99	65	400	350	10	1.0	−0.05
10.0	0.89	1.00	1.02	0.87	0.98	1.00	45	400	350	0	1.0	−0.05
15.0	0.90	1.00	1.01	0.89	0.99	1.00	5	400	350	0	−1.0	−0.05
20.0	0.90	1.00	1.00	0.89	0.99	1.00	25	400	350	0	−1.0	−0.05

TABLE V

Table of maximum $R_{gg}^{H}(\gamma\gamma)$ values for the Type II 2HDM with $m_H = 125$ GeV and associated R values for other initial and/or final states. The input parameters that give the maximal $R_{gg}^{H}(\gamma\gamma)$ value are also tabulated.

$\tan\beta$	$R_{gg\max}^{H}(\gamma\gamma)$	$R_{gg}^{H}(ZZ)$	$R_{gg}^{H}(b\bar{b})$	$R_{\mathrm{VBF}}^{H}(\gamma\gamma)$	$R_{\mathrm{VBF}}^{H}(ZZ)$	$R_{\mathrm{VBF}}^{H}(b\bar{b})$	m_h	m_A	$m_{H^\pm}$	m_{12}	$\sin\alpha$	$\mathcal{A}_{H^\pm}^{H}/\mathcal{A}$
1.0	1.99	3.24	0.52	0.71	1.16	0.19	125	500	500	100	1.0	−0.06
2.0	2.56	3.36	0.00	1.46	1.92	0.00	125	300	340	50	1.0	−0.06
3.0	2.73	3.29	0.00	1.97	2.37	0.00	125	300	320	50	1.0	−0.05
4.0	2.78	3.25	0.00	2.20	2.57	0.00	125	300	320	50	−1.0	−0.05
5.0	2.81	3.23	0.00	2.32	2.66	0.00	125	300	320	50	−1.0	−0.05
7.0	2.80	3.21	0.00	2.40	2.75	0.00	65	300	320	10	−1.0	−0.06
10.0	2.81	3.20	0.00	2.46	2.79	0.00	45	300	320	0	−1.0	−0.06
15.0	2.82	3.19	0.00	2.49	2.82	0.00	25	300	320	0	−1.0	−0.05
20.0	2.82	3.19	0.00	2.50	2.83	0.00	25	300	320	0	−1.0	−0.05

TABLE VI

Table of maximum $R_{gg}^{h+A}(\gamma\gamma)$ values for the Type I 2HDM with $m_h = m_A = 125$ GeV and associated R values for other initial and/or final states. The input parameters that give the maximal $R_{gg}^{h+A}(\gamma\gamma)$ value are also tabulated.

$\tan\beta$	$R_{gg\max}^{h+A}(\gamma\gamma)$	$R_{gg}^{h}(\gamma\gamma)$	$R_{gg}^{h+A}(ZZ)$	$R_{gg}^{h+A}(b\bar{b})$	$R_{\rm VBF}^{h}(\gamma\gamma)$	$R_{\rm VBF}^{h}(ZZ)$	$R_{\rm VBF}^{h}(b\bar{b})$	m_H	$m_{H^\pm}$	m_{12}	$\sin\alpha$	$\mathcal{A}_{H^\pm}^{h}/\mathcal{A}$
2.0	1.07	0.92	0.98	1.73	0.98	1.04	0.98	325	250	100	−0.5	−0.04
3.0	1.08	1.02	0.98	1.28	1.08	1.04	0.98	225	150	100	−0.4	0.01
4.0	1.35	1.33	0.99	1.21	1.24	0.93	0.99	225	90	100	−0.1	0.14
5.0	0.96	0.95	1.00	1.07	0.95	1.00	1.00	135	90	50	−0.2	−0.03
7.0	1.04	1.04	0.99	1.00	1.06	1.01	0.99	135	90	50	−0.2	0.02
10.0	0.91	0.90	0.81	0.77	0.99	0.89	0.81	175	150	50	−0.5	0.04
15.0	0.42	0.42	0.59	0.67	0.37	0.53	0.59	225	250	50	0.6	−0.17
20.0	1.31	1.31	1.00	1.00	1.30	0.99	1.00	225	90	50	−0.0	0.13

TABLE VII

Table of maximum $R_{gg}^{h+A}(\gamma\gamma)$ values for the Type II 2HDM with $m_h = m_A = 125$ GeV and associated R values for other initial and/or final states. The input parameters that give the maximal $R_{gg}^{h+A}(\gamma\gamma)$ value are also tabulated.

$\tan\beta$	$R_{gg\max}^{h+A}(\gamma\gamma)$	$R_{gg}^{h}(\gamma\gamma)$	$R_{gg}^{h+A}(ZZ)$	$R_{gg}^{h+A}(b\bar{b})$	$R_{\rm VBF}^{h}(\gamma\gamma)$	$R_{\rm VBF}^{h}(ZZ)$	$R_{\rm VBF}^{h}(b\bar{b})$	m_H	$m_{H^\pm}$	m_{12}	$\sin\alpha$	$\mathcal{A}_{H^\pm}^{h}/\mathcal{A}$
1.0	2.05	1.58	2.05	3.91	0.93	1.22	0.65	525	500	100	−0.5	−0.06
2.0	1.18	1.17	1.31	1.68	1.07	1.20	0.87	325	340	100	−0.4	−0.05
3.0	2.78	2.78	3.29	0.27	2.01	2.37	0.00	225	320	100	−0.0	−0.05
4.0	2.84	2.84	3.25	0.23	2.24	2.57	0.00	225	320	100	−0.0	−0.04
5.0	1.89	1.89	2.19	0.95	1.41	1.64	0.47	225	320	100	0.1	−0.05
7.0	0.04	0.04	0.06	2.85	0.01	0.02	0.75	325	320	100	0.6	−0.15
10.0	0.34	0.34	0.43	3.66	0.22	0.28	1.23	325	320	100	0.2	−0.08
20.0	2.89	2.89	3.19	8.03	2.57	2.83	0.00	225	320	50	−0.0	−0.04

We emphasize that a substantial enhancement of the $\gamma\gamma$ rate *is* possible for the h in Type I models without enhancing the ZZ rate. From Table II, we see that for $\tan\beta = 4$ and 20 the enhancement in the $\gamma\gamma$ channel is ~ 1.3 (for both gg fusion and VBF). It turns out that in these cases the total enhancement, $\sim 30\%$, is provided by the charged Higgs boson loop contribution to the $\gamma\gamma$-coupling. This maximum enhancement is achieved for $\sin\alpha \sim 0$, therefore, the coupling of the h to quarks and vector bosons is SM-like ($\beta \sim \pi/2$ and $\cos\alpha \sim 1$). The mass of the heavier Higgs boson is $m_H = 225$ GeV, which is within the reach of the LHC.

Using current data, the H will not be detected since $g_{HZZ} \propto \cos(\beta - \alpha)$ and $g_{Hb\bar{b},Ht\bar{t}} \propto \sin\alpha$ so that the H decouples from both vector bosons and fermions given that $\alpha \sim 0$ and $\beta \sim \pi/2$. The A will also be difficult to detect since it has no tree-level WW, ZZ coupling and the $Ab\bar{b}$, $At\bar{t}$ couplings, $\propto \cot\beta$, will be quite suppressed, especially at $\tan\beta = 20$.

From Table II, we observe that for $\tan\beta = 4$ and 20 the corresponding charged Higgs is light, $m_{H^\pm} = 90$ GeV, *i.e.* as small as allowed by LEP2 direct searches in $e^+e^- \to H^+H^-$. Searches for a light $H^\pm$ are underway at the LHC along the lines described in [17]. Currently, a charged Higgs yielding enhanced $h \to \gamma\gamma$ rates in gg fusion and VBF is still fully consistent with the data [18, 19].

3.2. Degenerate scenarios

One also needs to consider scenarios with mass degeneracy between m_h, m_H and m_A. The signal at 125 GeV can come from both h and H. It cannot be pure A since the A does not couple to ZZ. However, one can imagine that the $\mathcal{CP}$-even h or H and the A both have mass of 125 GeV. We will discuss further only the possibility of h and A degeneracy, as other cases are disfavored by the data (see [5]).

For the Type I model, we see from Fig. 2 and Table VI that $R_{gg}^{h+A}(\gamma\gamma)$ is significantly enhanced only for the same $\tan\beta = 4$ and $\tan\beta = 20$ values as in the case of having (only) $m_h = 125$ GeV and that the pseudoscalar contribution $R_{gg}^{A}(\gamma\gamma)$ turns out to be tiny. However, the contribution to the $b\bar{b}$ final state from the A *can* be substantial. This (unwanted) contribution to the $b\bar{b}$ final state from A production is apparent from the results for $R_{gg}^{h+A}(b\bar{b})$ in Table VI for $\tan\beta = 2$–4. In the end, only $\tan\beta = 20$ yields both an enhanced $\gamma\gamma$ rate, $R_{gg\,\max}^{h+A}(\gamma\gamma) = 1.31$, and SM-like rates for the ZZ and $b\bar{b}$ final states, $R_{gg}^{h+A}(ZZ), R_{gg}^{h+A}(b\bar{b}) \sim 1$. For this case, $\beta \simeq \pi/2$ and $\alpha = 0$ implying that the h couples to fermions and gauge bosons like a SM Higgs boson and the enhancement of $R_{gg\,\max}^{h+A}(\gamma\gamma)$ is due exclusively to the charged Higgs loop contribution to the $\gamma\gamma$ couplings.

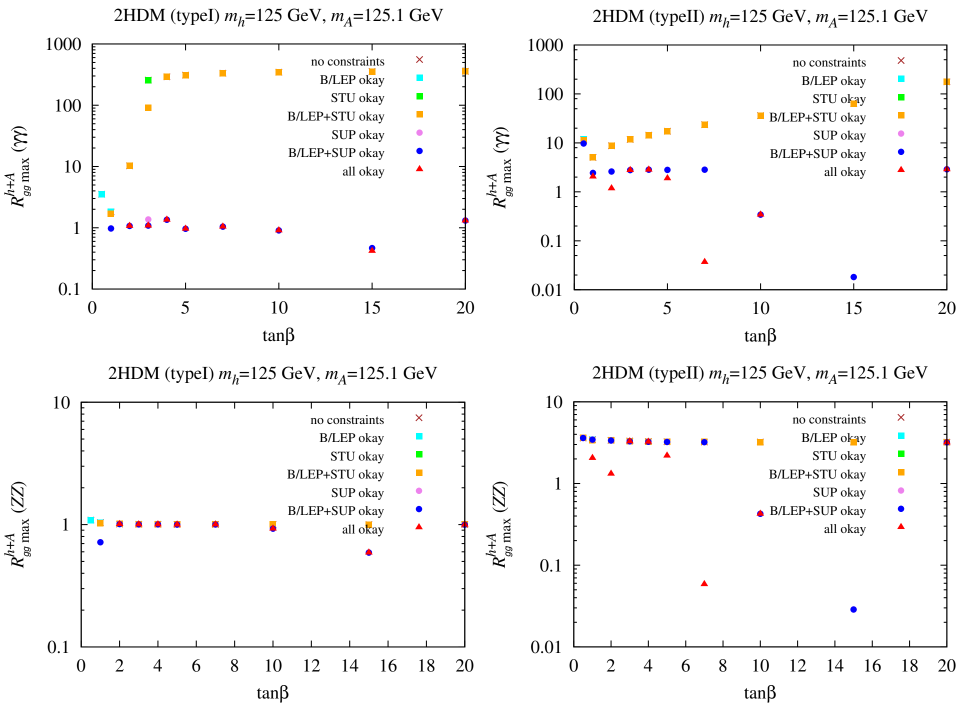

Fig. 2. $R_{gg}^{h+A}(\gamma\gamma)$ maximum values when $m_h = m_A = 125$ GeV as a function of $\tan\beta$ after imposing various constraints — see the figure legend. Corresponding $R_{gg}^{h}(ZZ)$ is shown in the lower panels.

For the Type II model, the enhancement of $R_{gg}^{h+A}(\gamma\gamma)$ is essentially the same as that for $R_{gg}^{h}(\gamma\gamma)$ for the case when only $m_h = 125$ GeV, reaching maximum values of the order of 2–3 (see Table VII). However, as in the pure $m_h = 125$ GeV case, a substantial enhancement of $R_{gg}^{h+A}(\gamma\gamma)$ is most often associated with $R_{gg}^{h+A}(ZZ) > R_{gg}^{h+A}(\gamma\gamma)$, as in the pure $m_h = 125$ GeV case (contrary to the LHC observations). But this is not *always* the case. Among the $m_h \sim m_A$ scenarios, we find 56 points in our parameter space for which $R_{gg}^{h+A}(ZZ) < 1.3$ and $R_{gg}^{h+A}(\gamma\gamma) > 1.3$. Unfortunately, for all those points the $\tau\bar{\tau}$ signal is predicted to be too strong, $R_{gg}^{h+A}(\tau\tau) \gtrsim 4$.

4. Conclusions

We have discussed the Type I and Type II 2HDMs with regard to consistency with a significant enhancement of the gluon-fusion-induced $\gamma\gamma$ signal observed at the LHC at ~ 125 GeV. Generically, we observe that the Type II model allows a maximal enhancement of the order of 2–3, whereas within the Type I model the maximal enhancement is limited to $\lesssim 1.3$.

However, we find that for Type II models a significantly enhanced $gg \to h \to \gamma\gamma$ signal is inconsistent with results in other channels. In the Type II model, the parameters that give $R^h_{gg}(\gamma\gamma) > 1.3$ are correlated with $R^h_{gg}(ZZ) > R^h_{gg}(\gamma\gamma)$, which is in contradiction with experimental results for $gg \to h \to ZZ \to 4\ell$. Similar statements apply to the case of the heavier H having a mass of 125 GeV. In the case of Type II models with approximately degenerate Higgs bosons at 125 GeV, we found that there exist theoretically consistent parameter choices for which $R^{h+A}_{gg}(\gamma\gamma) > 1.3$, while $R^{h+A}_{gg}(ZZ) < 1.3$. However, in these cases $R^{h+A}_{gg}(\tau\tau) \gtrsim 4$, a value is far above measured limits. Thus, the Type II 2HDMs cannot yield $R^{h+A}_{gg}(\gamma\gamma) > 1.3$ without conflicting with other observables. Nevertheless, definite conclusions require more precise data.

In the case of the Type I model, the maximal $R^h_{gg}(\gamma\gamma)$ is of the order of 1.3, as found if $\tan\beta = 4$ or 20 and the charged Higgs is light, $m_{H^\pm} = 90$ GeV. In these cases, $R^h_{gg}(ZZ)$ and $R^h_{gg}(\tau\tau)$ are of the order of 1. Thus, Type I models could provide a consistent picture if the LHC results converge to a modest enhancement for $R^h_{gg}(\gamma\gamma) \lesssim 1.3$.

In our analysis, we imposed all possible theoretical and experimental constraints. Vacuum stability, unitarity and perturbativity play the key role in limiting the maximal possible enhancement which, in the most interesting scenarios, is generated by the charged Higgs loop contribution to the Higgs to two photon decay amplitude.

This work has been supported in part by the U.S. DOE grant DE-FG03-91ER40674 and by the National Science Centre (Poland) as a research project, decision No. DEC-2011/01/B/ST2/00438. This work was supported by the Foundation for Polish Science International Ph.D. Projects Programme co-financed by the EU European Regional Development Fund. J.F.G. thanks the Galileo Galilei Institute and the LPSC Grenoble 2013 Higgs Workshop for support during the completion of this work.

REFERENCES

[1] G. Aad *et al.* [ATLAS Collaboration], *Phys. Lett.* **B716**, 1 (2012) [arXiv:1207.7214 [hep-ex]].

[2] S. Chatrchyan *et al.* [CMS Collaboration], *Phys. Lett.* **B716**, 30 (2012) [arXiv:1207.7235 [hep-ex]].

[3] P.M. Ferreira, R. Santos, M. Sher, J.P. Silva, *Phys. Rev.* **D85**, 035020 (2012) [arXiv:1201.0019 [hep-ph]].

[4] P.M. Ferreira, R. Santos, M. Sher, J.P. Silva, *Phys. Rev.* **D85**, 077703 (2012) [arXiv:1112.3277 [hep-ph]].

[5] A. Drozd, B. Grzadkowski, J.F. Gunion, Y. Jiang, *J. High Energy Phys.* **1305**, 072 (2013) [arXiv:1211.3580 [hep-ph]].

[6] D.S.M. Alves, P.J. Fox, N.J. Weiner, arXiv:1207.5499 [hep-ph].

[7] H.S. Cheon, S.K. Kang, arXiv:1207.1083 [hep-ph].

[8] S. Chang *et al.*, arXiv:1210.3439 [hep-ph].

[9] J.F. Gunion, Y. Jiang, S. Kraml, *Phys. Rev.* **D86**, 071702 (2012) [arXiv:1207.1545 [hep-ph]].

[10] D. Eriksson, J. Rathsman, O. Stal, *Comput. Phys. Commun.* **181**, 833 (2010); D. Eriksson, J. Rathsman, O. Stal, *Comput. Phys. Commun.* **181**, 189 (2010) [arXiv:0902.0851 [hep-ph]].

[11] J.F. Gunion, H.E. Haber, *Phys. Rev.* **D67**, 075019 (2003) [arXiv:hep-ph/0207010].

[12] J.F. Gunion, H.E. Haber, G.L. Kane, S. Dawson, *Front. Phys.* **80**, 1 (2000).

[13] G. Abbiendi *et al.* [OPAL Collaboration], *Eur. Phys. J.* **C27**, 311 (2003) [arXiv:hep-ex/0206022].

[14] G. Abbiendi *et al.* [OPAL Collaboration], *Eur. Phys. J.* **C40**, 317 (2005) [arXiv:hep-ex/0408097].

[15] G.C. Branco *et al.*, *Phys. Rep.* **516**, 1 (2012) [arXiv:1106.0034 [hep-ph]].

[16] I.F. Ginzburg, I.P. Ivanov, *Phys. Rev.* **D72**, 115010 (2005) [arXiv:hep-ph/0508020].

[17] M. Aoki *et al.*, *Phys. Rev.* **D84**, 055028 (2011) [arXiv:1104.3178 [hep-ph]].

[18] G. Aad *et al.* [ATLAS Collaboration], *J. High Energy Phys.* **1206**, 039 (2012) [arXiv:1204.2760 [hep-ex]].

[19] S. Chatrchyan *et al.* [CMS Collaboration], *J. High Energy Phys.* **1207**, 143 (2012) [arXiv:1205.5736 [hep-ex]].